Bani Asadi, Hossein; Madani, Zahraalsadat; Ajdary, Rubina; Rojas Gaona, Orlando; Seppälä, Jukka

Ascorbic acid-loaded polyvinyl alcohol/cellulose nanofibril hydrogels as precursors for 3D printed materials

Published in:
Materials Science and Engineering C

DOI:
10.1016/j.msec.2021.112424

Published: 01/11/2021

Document Version
Publisher's PDF, also known as Version of record

Materials Science & Engineering C 130 (2021) 112424

Contents lists available at ScienceDirect

Materials Science & Engineering C

journal homepage: www.elsevier.com/locate/msec

Ascorbic acid-loaded polyvinyl alcohol/cellulose nanofibril hydrogels as precursors for 3D printed materials

Hossein Baniasadi [a], Zahraalsadat Madani [a], Rubina Ajdary [b], Orlando J. Rojas [b,c], Jukka Seppälä [a,*]

[a] Polymer Technology, School of Chemical Engineering, Aalto University, Kemistintie 1, 02150 Espoo, Finland
[b] Department of Bioproducts and Biosystems, School of Chemical Engineering, Aalto University, P.O. Box 16300, FIN-00076 Aalto, Espoo, Finland
[c] Bioproducts Institute, Department of Chemical and Biological Engineering, Department of Chemistry and Department of Wood Science, University of British Columbia, 2360 East Mall, Vancouver, BC V6T 1Z3, Canada

ARTICLE INFO

Keywords:
Direct ink writing
Cellulose nanofibrils
Polyvinyl alcohol
Hydrogels
Shear-thinning

ABSTRACT

We proposed a simple method to process hydrogels containing polyvinyl alcohol and cellulose nanofibrils (PVA/CNF) to prepare volumetric architectures by direct ink writing (DIW). The presence of CNF in the aqueous PVA suspensions conferred rheology profiles that were suitable for extrusion and solidification in pre-designed shapes. The viscoelastic behavior of the hybrid inks enabled precise control on processability and shape retention, for instance, as demonstrated in multilayered lattice structures of high fidelity. After lyophilization, the obtained 3D-printed hydrogels presented a very high porosity, with open and interconnected pores, allowing a high-water uptake capacity (up to 1600%). The mechanical strength of the composite 3D-printed materials matched those of soft tissues, opening opportunities for skin applications. As such, drug-loaded samples revealed a controlled and efficient delivery of an antioxidant (ascorbic acid) in PBS buffer media at 23 °C (~80% for 8 h). Altogether, PVA/CNF hydrogels were introduced as suitable precursors of 3D-lattice geometries with excellent physical and mechanical characteristics.

1. Introduction

Additive manufacturing enables customized fabrication of 3D structures directly from computer-aided designs. Through the layer-by-layer deposition, this technique allows the development of unique structures that are otherwise challenging to produce by other processing routes [1,2]. Inkjet-, light- and extrusion-based 3D printing are among the most commonly cited 3D printing techniques. Therein, extrusion-based 3D printing has become popular given its availability and ease of use. For instance, it can be carried out with optional material melting. Meanwhile, 3D bioplotting, robocasting, and direct ink writing (DIW) are commonly used printing techniques that do not require thermal processing [3]. In DIW, a syringe with a nozzle moves across a surface and dispenses an ink [4–6]. This technique allows constructs with sophisticated 3D architectures at ambient conditions and has gained attention for its suitability for hydrogel printing where temperature-sensitive components are ideally utilized [7–9]. The printing parameters are selected to yield solid porosity and pore size distribution, ideal for biomedical applications [2]. However, not all hydrogels can be used as inks for DIW. For instance, they must exhibit a viscoelastic response to the applied pressure and present a shear-thinning viscosity, e.g., to allow extrusion from a nozzle to yield 3D structures through layer-by-layer deposition [3,10].

Hydrogels are three-dimensional polymeric networks that can swell in water without dissolution. They can be biodegradable and can be designed to display gas and water vapor permeability, as well as to produce porous structures, enabling uses as carriers for drugs, growth factors, and cells. Moreover, the viscoelastic properties of hydrogels can be precisely configured according to sensitive environmental conditions. Proper hydrogel compositions can mimic the extracellular matrix (ECM) and exhibit mechanical properties similar to soft tissues. As such, hydrogels have found widespread use in biomedical applications, including contact lenses, drug, and gene delivery, tissue engineering, artificial implants, and wound dressing [11–14].

Polyvinyl alcohol (PVA) is one of the most widely used polymers given its properties, including inherent nontoxicity, biocompatibility, non-carcinogenicity, desirable physical characteristics, adjustable mechanical properties, thermal stability, biodegradability, and a high

* Corresponding author.
E-mail address: jukka.seppala@aalto.fi (J. Seppälä).

https://doi.org/10.1016/j.msec.2021.112424
Received 28 June 2021; Received in revised form 23 August 2021; Accepted 5 September 2021
Available online 11 September 2021

degree of swelling in aqueous solutions [15–17]. PVA exhibits a strong hydrophilic and hydrogen bonding character attributed to the abundant -OH groups that exist in its structure, enabling the facile formation of gels that display high physical stability [18,19]. Compared to other available biodegradable polymers, such as poly(lactic-*co*-glycolic acid), polycaprolactone, and polyglycolide, PVA is an inexpensive and widely available polymer. Moreover, it is an FDA-approved biomaterial [20]. However, low viscosity and poor viscoelastic properties have restricted its application in DIW to develop customized structures [5,21].

Few reports exist on the DIW of PVA hydrogels. In one of the recent efforts, Meng et al. [21] successfully printed PVA/graphene oxide-hydroxyapatite (GO-HA) hydrogels through the DIW technique. They investigated the influence of the concentration and composition of PVA on the rheological behavior, printability, and compressive and tribological properties of the developed hydrogels. The hydrogels' printing accuracy and their promising potential for precisely customized repair of artificial cartilage were discussed. Similarly, Jiang et al. [5] reported DIW of hybrid hydrogel inks composed of PVA and κ-carrageenan. They revealed the outstanding rheology of the developed hydrogels, and their excellent mechanical properties, which arose from freezing and thawing processes. Furthermore, they proved excellent cytocompatibility of the printed samples and offered them for tissue engineering, drug delivery, bone regeneration, and implant medicine.

Another important component in DIW, cellulose nanofibrils (CNF), has been considered given that it is a natural polysaccharide with a native crystalline structure. It displays superb mechanical properties, high surface area, excellent biocompatibility, good biodegradability, and high chemical resistance. Therefore, CNF has been extensively incorporated into various polymer matrices, including those for biomedical applications. [22,23]. Our previous studies confirmed the excellent viscoelastic properties of CNF hydrogels and their outstanding potential for DIW [24–27]. Accordingly, we study the printability of PVA/CNF hydrogels with different compositions used to build tailored structures by the DIW technique. Ascorbic acid, a well-known water-soluble molecule, was incorporated for its attributes in biomedical applications [28,29]. The hydrogen bonds formed between PVA and CNF and their similar chemistry resulted in good interfacial adhesion and shear-thinning behavior, which enabled the inks to form complex and tunable architectures through DIW. The biocompatible 3D structures are demonstrated for their excellent promise as far as their mechanical performance and controlled drug release properties.

2. Experimental

2.1. Materials

Polyvinyl alcohol (Mw 31,000–50,000, 98–99% hydrolyzed), sodium chloride, sodium bromide, sodium hypochlorite, sodium hydroxide, and L-Ascorbic acid (99%) were purchased from Sigma-Aldrich.

2.2. Ink preparation

PVA (10 wt%) was dissolved into the water at 90 °C with vigorous stirring under a condenser and then cold down at ambient temperature. TEMPO-CNF (1.7 wt%) was produced similar to a method reported in our previous work [30]. Afterward, the different mass ratios of PVA solution and CNF suspension were mixed gently using an IKA Ultra Turrax T25 digital homogenizer for 10 min at 12000 rpm. The obtain ink was then centrifuged at 3000 rpm for 3 min to remove air bubbles. The total amount of dried composite was fixed at 3 wt%. The selected solid content was obtained by monitoring the filaments' quality as was extruded from the printer's nozzle. The mass ratios of PVA/CNF were selected as 1/0.6, 1/0.8, and 1/1, and the composite inks were coded as P1T0.6, P1T0.8, and P1T1, respectively. The incorporation of CNF was found to be critical to ensure the 3D printability of the ink. Therefore, the 1:0.6 ratio was the minimum possible amount of CNF to guarantee ink printing and obtain structures with suitable fidelity.

2.3. Drug loading

Ascorbic acid was loaded into the samples through two different methods. In the first method, ascorbic acid was added directly to the ink, and the system was mixed under gentle mixing at room temperature. The amount of loaded drug was 10% of the total dry weight of PVA and CNF [31]. In the second method, the indirect approach, the lyophilized 3D-printed sample was incubated in an ascorbic acid solution. Approximately 0.075 g of the sample was added into 25 mL of ascorbic acid solution with a concentration of 10 mg L^{-1} [32], and the system was agitated at 23 °C for 1 h. Afterward, the sample was removed, lyophilized, and the amount of loaded drug was determined spectrophotometrically. It was approximately 5%.

2.4. Direct ink writing

A BIOX (CELLINK, Sweden) printer equipped with a pneumatic printhead was used for ink DIW (with and without drug). The ink was loaded to a 3 mL clear pneumatic syringe and extruded throughout a blunt needle (840 μm tip diameter) using 40 kPa pressure. Two different geometries, including disk-shape (15 mm and 25 mm diameter) and lattice-shaped, were printed with infill density of 100% and 20%, respectively. The latter was used to illustrate the ability of ink to be printed more on complex and tailored architectures. The samples were freeze-dried at −40 °C for 48 h to improve their mechanical properties through PVA re-crystallization.

2.5. Characterization

2.5.1. Rheology

The rheological behavior of the prepared inks was investigated using a rotational rheometer with parallel plate geometries (PP25 and CP25) (Anton Paar MCR 301, Austria) at 23 °C. CP25 geometry was utilized to measure the apparent shear viscosity of the ink (η) as a function of shear rate (γ) between 0.01 and 1000 s^{-1} at a fixed gap of 49 μm. The power-law equation (Eq. (1)) was used to investigate the relationship between η and γ.

$$\eta = K.\gamma^{n-1} \tag{1}$$

where K and n describe the consistency index and flow index, respectively. The exponent (n) was used to evaluate the flow properties of the inks, where $n < 1$ indicates shear thinning, $n > 1$ illustrates shear thickening, and $n = 1$ represents Newtonian flow [33].

Afterward, a strain sweep test was done between 0.01 and 100% using PP25 geometry and an oscillatory logarithmic interval at fixed frequency of 10 rad.s^{-1} to determine the linear viscoelastic region. The storage and loss moduli were then recorded in the frequency range from 0.1 and 100 rad.s^{-1} at a fixed strain of 0.1% using PP25 geometry. The inks' yield stress (τ_y) was evaluated through a stress sweep test, where the stress increased logarithmically from 0.1 to 10^3 Pa at a constant frequency of 10 rad.s^{-1}. It was then compared with the maximum shear stress generated within the nozzle (τ_{max}), the shear rate at the nozzle wall, to investigate the flowability of the inks under the printing conditions. The inks would be expected to print if τ_{max} is high enough to overcome τ_y. τ_{max} be calculated from the following equation, in which ΔP is the maximum pressure applied at the nozzle (40×10^3 Pa) and r and L are the nozzle radius (420×10^{-6} m) and the nozzle length (3.175×10^{-2} m), respectively [34–36].

$$\tau_{max} = \frac{\Delta P.r}{2L} \tag{2}$$

The strain and frequency sweep tests were also conducted for 3D-printed samples using PP25 geometry at a fixed gap of 4 mm with the

same test conditions previously explained for the inks. The samples were equilibrated in water prior to the testing. The obtained storage modulus (G′) was further employed to calculate the sample's elastic modulus (E) through Eq. (3).

$$E = 2G^{'}(1+2\nu) \quad (3)$$

The Poisson ratio (ν) was set at 0.5 since the mechanical behavior of the swollen sample can be considered similar to that of rubber-like materials [37].

2.5.2. Shrinking behavior of the 3D-printed sample

The volumetric shrinkage was calculated by comparing the 3D-printed samples' apparent volume before and after freeze-drying.

2.5.3. Morphological study

The morphology of hydrogels was studied using a Zeiss Sigma VP scanning electron microscope (SEM). The freeze-dried 3D-printed hydrogel was cut to a small piece; its surface and cross-section area were sputter-coated with gold-palladium (LECIA EM ACE600 sputter coater) and were subjected to SEM imaging. The pore size was measured using ImageJ software for approximately 100 pores selected from the different SEM image areas [38]. The mean value ± error of the mean was reported as an average pore size of the sample.

2.5.4. The swelling capacity of the hydrogel

The swelling behavior of the hydrogel was studied by monitoring the water absorption of the dried sample for 24 h. The freeze-dried printed hydrogel was weighted (m_0) and immersed in a PBS solution. It was taken out periodically; the surface buffer solution was removed using tissue paper and weighted immediately (m_i). The swelling ratio was calculated via Eq. (4).

$$Swelling\ ratio\ (\%) = \frac{m_i - m_0}{m_0} \times 100 \quad (4)$$

2.5.5. Weight loss of the hydrogel

The hydrogel degradation was measured according to its weight loss into the PBS solution for 7 days. The freeze-dried 3D-printed sample was weighted (m_0) and immersed in a PBS solution. It was taken out at specific times, thoroughly vacuum dried at 40 °C, and weighted again (m_d). The weight loss was calculated via Eq. (5).

$$Weight\ loss\ (\%) = \frac{m_0 - m_d}{m_0} \times 100 \quad (5)$$

2.5.6. Porosity

The porosity of the hydrogel was measured according to the method reported by Pan et al. [39]. The weight of the lyophilized hydrogel (m_i) and its apparent volume (V) were measured. It was then immersed in ethanol to saturate. The weight of saturated hydrogel was measured (m_{sat}). Porosity was obtained from Eq. (6), in which ρ is the density of ethanol (0.789 g/mL).

$$\Phi(\%) = \frac{m_{sat} - m_i}{\rho \times V} \times 100 \quad (6)$$

2.5.7. Compression test

The compression stress-strain curves were obtained using an Instron Universal testing machine model 5944 with a 50 N load cell. All 3D-printed samples were equilibrated in water; then compressed up to approximately 70% strain with a constant rate of 0.5 mm.min^{-1} in controlled conditions (T = 23 °C and relative humidity = 50%). The compressive modulus and compressive stress at 10%, 30%, and 60% strain were compared for all samples.

2.5.8. Fourier transform infrared (FTIR) spectrometry

The FTIR spectra were recorded from 4000 and 500 cm^{-1} using a PerkinElmer FTIR with an ATR instrument at a resolution and scan number of 4 cm^{-1} and 32, respectively.

2.5.9. Drug calibration curve and release

A certain amount of ascorbic acid was dissolved in PBS to produce a standard solution of 100 ppm. Then, approximately 4.0 mL solution was taken and scanned from 200 to 900 nm with a Shimadzu spectrophotometer model UV-2550 to find the λ_{max} (peak wavelength of spectra) of ascorbic acid. It was 295 nm, in good agreement with that reported in the literature at pH 7.4 [40]. Afterward, three concentrations of the standard solution, including 25, 50, and 75 ppm, were prepared, their absorbance was read at 295 nm, and the data was used to construct the calibration curve (Fig. S1).

The ascorbic acid-loaded hydrogel was dried thoroughly at 40 °C using a vacuum oven and then weighted (m_0). After that, the sample was immersed in the PBS solution at 23 °C and mixed for 24 h. The sample solution (4 mL) was withdrawn at different time points, including 10 min, 20 min, 30 min, 1 h, 2 h, 3 h, 4 h, 6 h, 8 h, 10 h, 12 h, and 24 h, and the same volume of fresh PBS was replaced. The collected sample solution absorbance was determined using the UV–vis spectrophotometer at a wavelength of 295 nm. The ascorbic acid released from the sample (C_i) was back-calculated against the calibration curve and the cumulative percentage release at specific time points using the following equation [41].

$$Cumulative\ release(\%) = \frac{C_i V_t + V_s \sum_{2}^{n} C_{i-1}}{W_t} \times 100 \quad (7)$$

where C_i is the concentration of drug in the released solution at the time i, V_t is the total volume of the released solution, V_s is the sample solution volume (4 mL), and W_t is the total amount of ascorbic acid in the sample.

2.6. Statistical analysis

Each experiment was carried out at least in three replicates, and the average value ± standard error of the mean was reported. The mean value was compared by one-way analysis of variance (ANOVA), and *P*-value less than 0.05 was considered statistically significant.

3. Results and discussion

3.1. Evaluation of ink printability and viscoelastic performance

Ink consistency, including shear-thinning properties, yield stress, and viscoelasticity, are critical in DIW. The gel strength rate during printing and the resolution and shape fidelity of the structure after printing are also important design parameters [42,43]. Accordingly, the viscosity and viscoelastic behavior of the inks were investigated. Fig. 1a illustrates the ink viscosity trend versus the shear rate at 23 °C. On one side, the viscosity range of the inks was in a suitable range for extruder-based 3D printers. In addition, a significant reduction of ink viscosity was observed upon increasing the shear rate, indicating a shear-thinning behavior. This is favorable for DIW since the ink can easily extrude without clogging the nozzle tip due to the high shear rates subjected to the 3D printing materials. Furthermore, the shape can be preserved after deposition, with each layer shows high fidelity, without any deformation due to recovering viscosity after removing the stress/shear rate [44,45]. Although the viscosity increased with CNF content, the exponent n calculated in Eq. (1) (Fig. S2a) suggested that the amount of CNF did not significantly affect the shear-thinning behavior of the ink. It is also worth mentioning that a 10 wt% PVA solution displayed the slight shear-thinning behavior with a final viscosity of approximately 120 mPa.s (Fig. S2b) [5]; therefore, the observed rheological performance of the composite inks could be attributed to the incorporation of CNF.

The inks were further subjected to an increasing oscillating strain at a

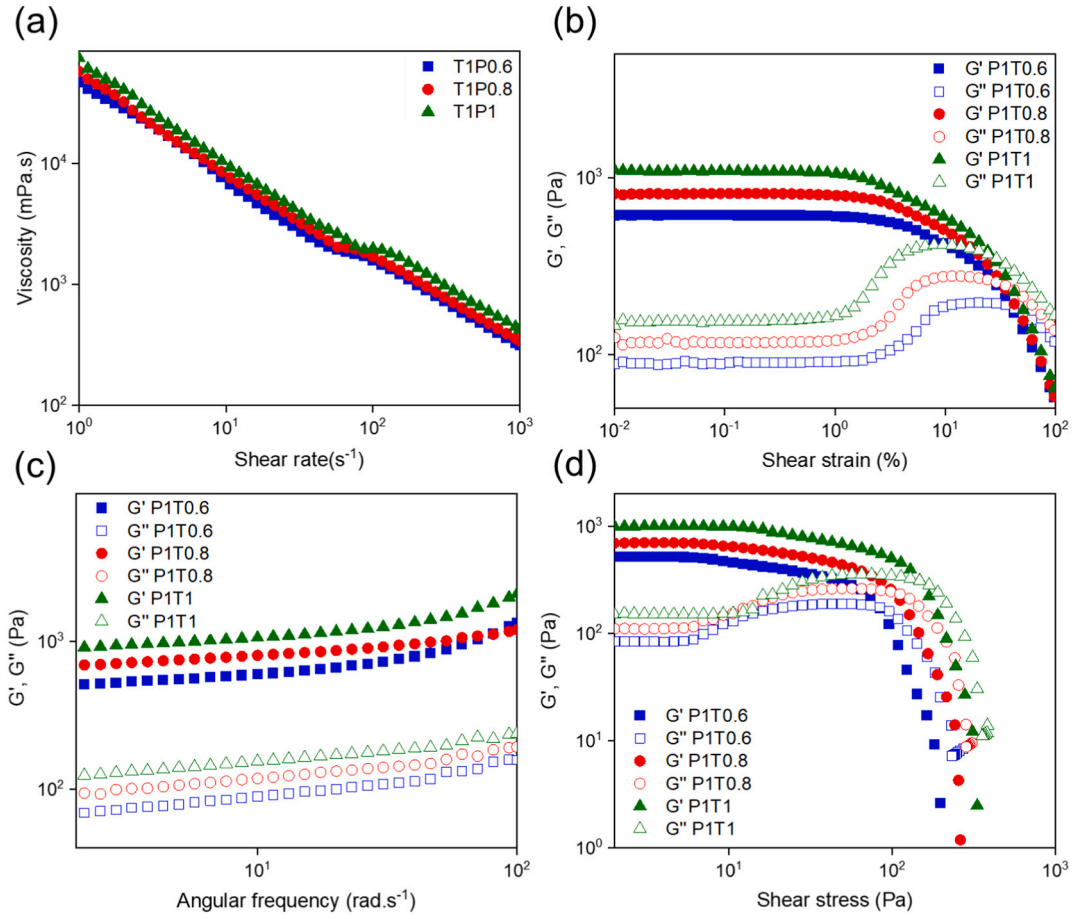

Fig. 1. Viscoelastic properties of the inks at 23 °C. (a) apparent viscosity versus the shear rate from 0.01 to 1000 s^{-1}, (b) G′ and G″ versus strain rate from 0.01 to 100% at a fixed frequency of 10 rad.s^{-1}, (c) G′ and G″ versus frequency from 0.01 to 100 rad.s^{-1} at a fixed strain rate of 0.1%, and (d) G′ and G″ versus shear stress from 0.1 to 1000 Pa at a fixed frequency of 10 rad.s^{-1}. Viscoelastic properties of the 3D-printed samples at 23 °C.

constant frequency of 10 rad.s^{-1} to quantify the range of linear viscoelastic behavior. Fig. 1b demonstrates the trend of G′ and G″ versus strain rate at 23 °C. The curves of both moduli were flat at low strain values (approximately less than 1%); thus, the amplitude of 0.1% was considered the linear viscoelastic region of the inks. Furthermore, the threshold upon which linear to non-linear transition occurred slightly decreased upon increasing CNF content, indicating the formation of a robust structure. This trend was in agreement with the data are shown by Abbasi et al. [46], in which samples with a more robust network collapsed at smaller deformations. When the strain amplitude surpassed 1%, G′ dropped dramatically while G″ first increased then decreased. The peak of the G″ curve was varied between 10 and 17% depending on CNF content, attributing to the structural instability of the network, similar to the Panye effect that is a universal phenomenon occurring in the rubber filled with particles under an increasing strain amplitude [47]. On the other hand, as the strain increased, G″ prevailed over G′ for all inks, indicating a flow point due to the network structure yielding and failure. In other words, the network structure started to behave as a non-Newtonian shear-thinning fluid [43].

Frequency sweeps were performed in the range of 0.01–100 rad.s^{-1} at a shear strain of 0.1% to evaluate the inks' strength. The results of the oscillation frequency sweep test are presented in Fig. 1c. For all inks, G′ was always significantly higher than G″ corresponding to relatively low tan δ values (Fig. S3), and there was no crossover. Such a low value of tan δ, which was in the range of 3D printable material [44], indicated that the system's elasticity increased, and consequently, a solid-like behavior was dominant. In addition, both G′ and G″ increased with CNF content, confirming the reinforcing effect of well-distributed high aspect ratio nano and microfibrils cellulose into the PVA matrix. The formation of a physical network by the chain entanglements of CNF has also been reported as a reason for such improvement [35,48]. The obtained G′ and G″ values were in the ranges previously reported for PVA/cellulose nanocrystals (CNC) [46], starch/PVA/nanosilver [49], and PVA/cellulose nanofibril/lignin [50] hydrogels.

The yield stress (τ_y) is another critical parameter determining the printing quality during and after the 3D printing process. The materials with adequate yield stress and a higher storage modulus than the loss modulus demonstrate a significant self-supporting structure [44]. Accordingly, the storage and loss moduli trend against shear stress was investigated at a fixed frequency of 10 rad.s^{-1} (Fig. 1d). The yield stress, the minimum required stress for material flow, was determined from the amount of stress at the intersection of the G′ and G″. At low stress values, G′ was significantly higher in all inks than G″, suggesting that the inks had significant stability to hold themselves in the nozzle before applying the external pressure and printing [51]. By further increasing the applied stress above the linear viscoelastic region, the yield stress point was obtained as G′ intersected G″ revealing the material flow from the nozzle. τ_y values were 82.5 Pa, 102.6 Pa, and 147.3 Pa for P1T0.6, P1T0.8, and P1T1 samples, respectively, indicating a systematic increase upon increasing CNF content. It might be attributed to the CNF reinforcing effect as already observed at the frequency sweep test. On the other side, τ_y values were compared with τ_{max}, the maximum shear stress generated within the nozzle. It was calculated as 265 Pa using Eq. (2), which was significantly higher than inks' τ_y values, revealing that the applied pneumatic pressure was high enough to overcome the shear yield stress; therefore, CNF could be aligned, and all inks could be

printed [34,35].

3.2. Direct ink writing and shrinkage behavior of PVA/CNF hydrogels

The water trapped inside the hydrogels may make them unstable and prone to collapse during printing, challenging shape fidelity after 3D printing and reducing dimensions as compared to the original pattern after drying [34,51]. Accordingly, the deposition of the inks and the shape stability was monitored visually during and after printing. In addition, the dimensional changes of the printed samples were measured after printing and after lyophilization and presented as the samples' shrinkage. Three different grid patterns with an infill density of 20% were printed using the developed inks with a 20 G needle. Fig. 2 illustrates a 3D model and digital photographs of the printed samples after printing and freeze-drying. Under the printing conditions, all inks revealed excellent flowability attributing to their significantly lower yield stress values than the applied stress on the nozzle tip as well as to their shear-thinning viscosity. They extruded smoothly during printing while no needle clogging and liquid spreading, as the common challenges in DIW [52], were observed. Accordingly, good printability with high fidelity and fair resolution and uniform filament diameter of 865 ± 35 μm were achieved; they were acceptable matches with nozzle diameter, ensuring excellent control over the 3D-printed objects [24]. Each layer remained individualized, did not collapse, and appropriately maintained its uniform structure. A short ink recovery time was expected given the relatively high viscosity of the hydrogel after shearing

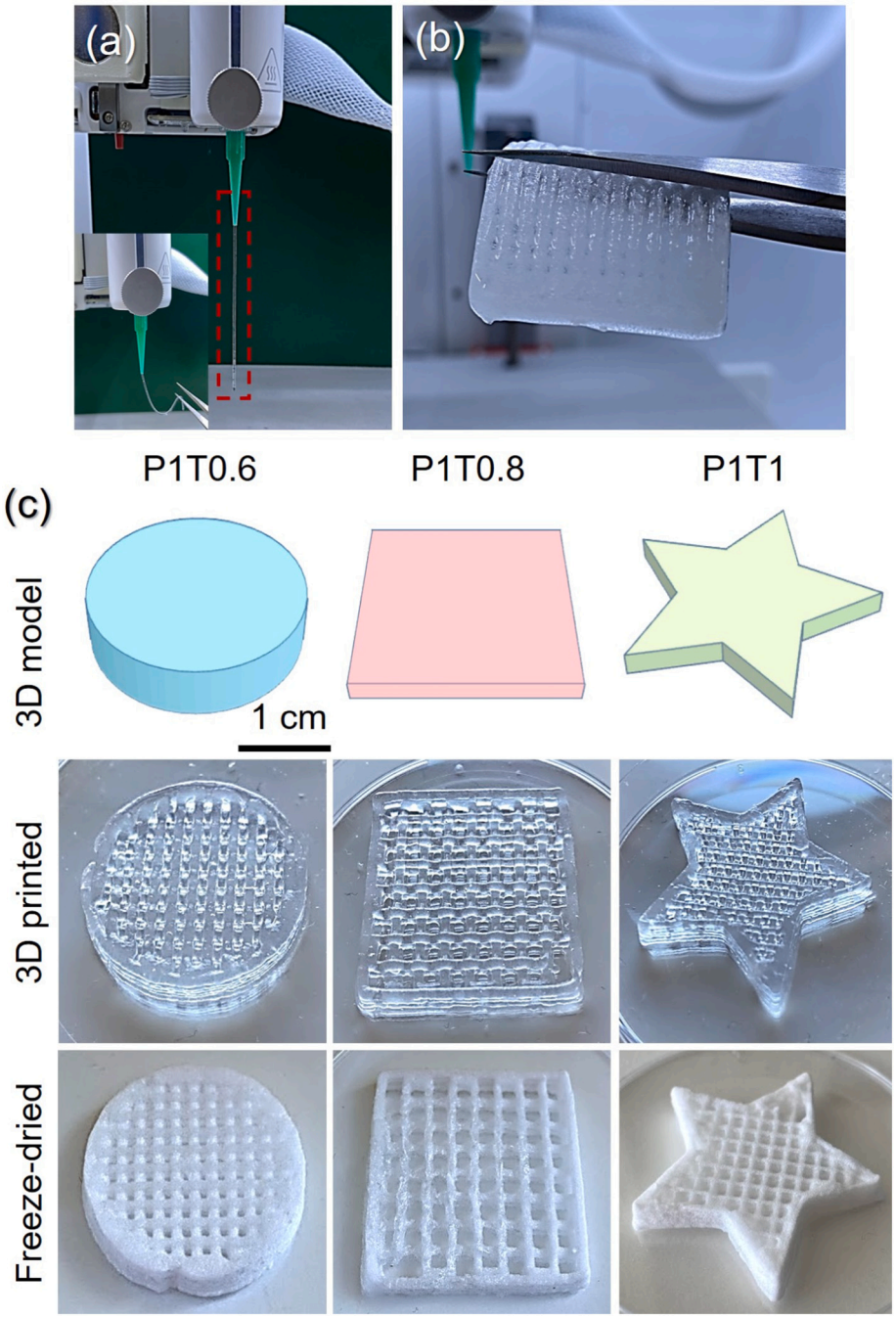

Fig. 2. (a) the extrusion of the hydrogel in filament form and (b) the rehydrated structure after 3D printing and lyophilization. (c) 3D model, 3D-printed structures, and freeze-dried samples.

in the nozzle, which is vital for building 3D architectures through layer-by-layer deposition methods [53]. The intermolecular hydrogen bonding between PVA and CNF hydrogels are some of the reasons for the high structural stability. It is worth noting that the 3D-printed samples were soft, flexible, and mechanically strong; for instance, they were suitable for handing, making them attractive for applications such as wound dressings [54].

The shrinkage measurement results are summarized in Table 1. All samples displayed minimal dimensional shrinkage (less than 10%) and well-maintained structures, much lower than that reported for PVA/CNC [55] and *aloe vera*/cellulose nanofibril [6] hydrogels. Such a low dimensional shrinkage could be attributed to the production of dried templates, called cryogels, inside the sample during drying, which positively retaining the original shape and volume. In other words, a rigid structure was formed after removing the trapped water through the sublimation of ice crystals during lyophilization that consequently limited the structural shrinkage [56].

3.3. Microstructure and porosity of the lyophilized 3D-printed hydrogels

The porosity and pore size of 3D hydrogels are crucial aspects governing hydrogel property and directly influence their performances during biomedical applications [37,57]. They are also crucial in wound healing; a proper pore size guarantees the air permeability of the wound, while the excessive pore diameter increases the risk of bacterial contamination [58,59]. Accordingly, the microstructures of hydrogels were thoroughly characterized. The SEM images taken from the surface and cross-section area of the lyophilized hydrogels are depicted in Fig. 3. All lyophilized hydrogels showed a porous, rough surface structure and possessed a similar hierarchical porous and uniform interconnected network. Furthermore, no evidence of the collapse of the pores was observed, which could be due to the entanglement between PVA and CNF, and less shrinkage during freeze-drying resulted in better shape fidelity [3].

The hierarchical structure suggests strong interactions between the compounds, resulting in significant hydrophilicity and desirable mechanical properties of the hydrogel [60]. Open pores and interconnected networks are favorable for tissue engineering applications since they can facilitate cell migration, attachment, and proliferation within the gel as well as support nutritional transfer [61]. Moreover, porous architecture with interconnected holes is favorable for wound dressing hydrogels because it provides a high surface area that would absorb wound exudates and easily exchange oxygen and nutrients through its highly porous structures [62]. It is also noteworthy that no evidence of CNF aggregation or two phases formation was detected in SEM images, demonstrating that the CNF dispersed well in the PVA matrix in all hydrogels, and there was excellent compatibility between the two components. Moreover, in contrast to what was previously reported by Zhang et al. [63], no disorganized structures were observed at high CNF content.

The microstructure was further investigated by measuring the porosity and average pore size of the developed hydrogels. The results are summarized in Table 1. All freeze-dried 3D-printed samples revealed porosity higher than 80%, which did not change significantly upon increasing CNF content. The measured porosity compared closely with values reported for polyvinyl alcohol formaldehyde-*g*-poly(2-(dimethylamino)ethyl methacrylate) [64], PVA/bacterial cellulose/nanosilver [65], and PVA/agarose [66] hydrogels. It has been reported the polymer concentration is one of the factors that affect porosity [67]. Therefore, since the polymer was fixed in all hydrogels (3 wt%), they illustrated almost the same porosity. On the other side, the pore size of all samples was in an appropriate range for tissue engineering and wound dressing applications [58,68]. Furthermore, it slightly increased with cellulose concentration due to its higher water uptake capacity, as shown in the following. As the amount of absorbed water increases, the space occupied by the water becomes more extensive, and consequently, the pore size of the hydrogel increases after freeze-drying [69].

Table 1
Shrinkage, porosity, pore size, swelling ratio, and weight loss of the samples.

Sample	Shrinkage, %	Porosity, %	Pore size, μm	Swelling ratio, %[a]	Weight loss, %[b]
P1T0.6	9 ± 0.8	82 ± 5.3	33.94 ± 12.84	994 ± 77	3.1 ± 0.65
P1T0.8	7 ± 0.5	83 ± 6.7	36.86 ± 13.78	1047 ± 123	2.6 ± 0.44
P1T1	6 ± 1.1	88 ± 4.8	40.84 ± 19.10	1614 ± 198	2.9 ± 0.3

[a] After 24 h.
[b] After 5 days.

3.4. Swelling behavior and weight loss

The swelling property of hydrogels is vital for tissue engineering applications; it forms 3D structures favorable for cell infiltration and migration and facilitates the penetration of the active ingredients into the target site. Furthermore, it is favorable for wound healing because it keeps the moisture of the wound and prevents the formation of dry scabs, and avoids any pain during dressing changes [70,71]. Fig. 4a summarizes the swelling ratios of the lyophilized 3D-printed samples at PBS solution for 24 h at 23 °C. The swelling ratio of all hydrogels increased drastically within 1 h; then, it reached a plateau approximately after 6 h due to the saturation of the samples. The equilibrated swelling ratio of all samples is provided in Table 1. This relatively high water absorption capacity, in good agreement with other reports related to PVA-based hydrogels [48,72,73], was due to abundant free hydroxyl groups of PVA and CNF that turned into their ion forms and formed hydrogen bonding with water molecules leading to swelling hydrogels [74,75]. Upon increasing the CNF content, the swelling ratio increased gradually, which might be due to the presence of the hydrophilic functional groups, like carboxylic acid functionalities, on the cellulose fibrils surfaces [72,75]. Nevertheless, the digital photographs of freeze-dried and rehydrated samples (Fig. 4c) confirmed the stability of all samples 24 h after immersing in water attributed to the support provided by high aspect ratio micro- and nano-size fibrils.

The weight loss of the hydrogels, which was evaluated in PBS solution, is demonstrated in Fig. 4b. Furthermore, the weight loss values of all samples after 7 days are summarized in Table 1. All the hydrogels revealed minor mass losses around 3% after 7 days due to the intrinsic very low degradation of PVA and CNF at ambient conditions [76,77]. It has been reported that biodegradation of PVA-based hydrogels takes place in the enzymatic environment. For instance, approximately 45% degradation was reported by Date et al. [78] for agarose/PVA hydrogels in the egg lysozyme medium (1.5 μg/mL) at 37 °C. On the other hand, significant degradation of PVA-based hydrogels has also been reported under ambient conditions: Hemmatgir et al. [79] showed 30% degradation for polyethylene glycol diacrylate/PVA/tragacanth gum hydrogel after 7 days in PBS solution. Such a high degradation rate in enzyme-free media could be due to the poor crosslinking process, which caused a high amount of polymer release during the test time. To better demonstrate the high stability of the samples in PBS solution, the samples were removed from PBS solution 7 days after immersion, freeze-dried, and subjected to digital photography (Fig. 4c). The photos of the freeze-dried sample before the swelling test and 7 days after immersion indicated its high stability in PBS solution.

3.5. Mechanical properties of the lyophilized printed samples

The viscoelastic performance of the printed lyophilized samples was investigated through rheology measurements. The samples were equilibrated in water before testing. Fig. 5a presents the strain sweep test results executed between 0.01 and 100% at a constant frequency of 10

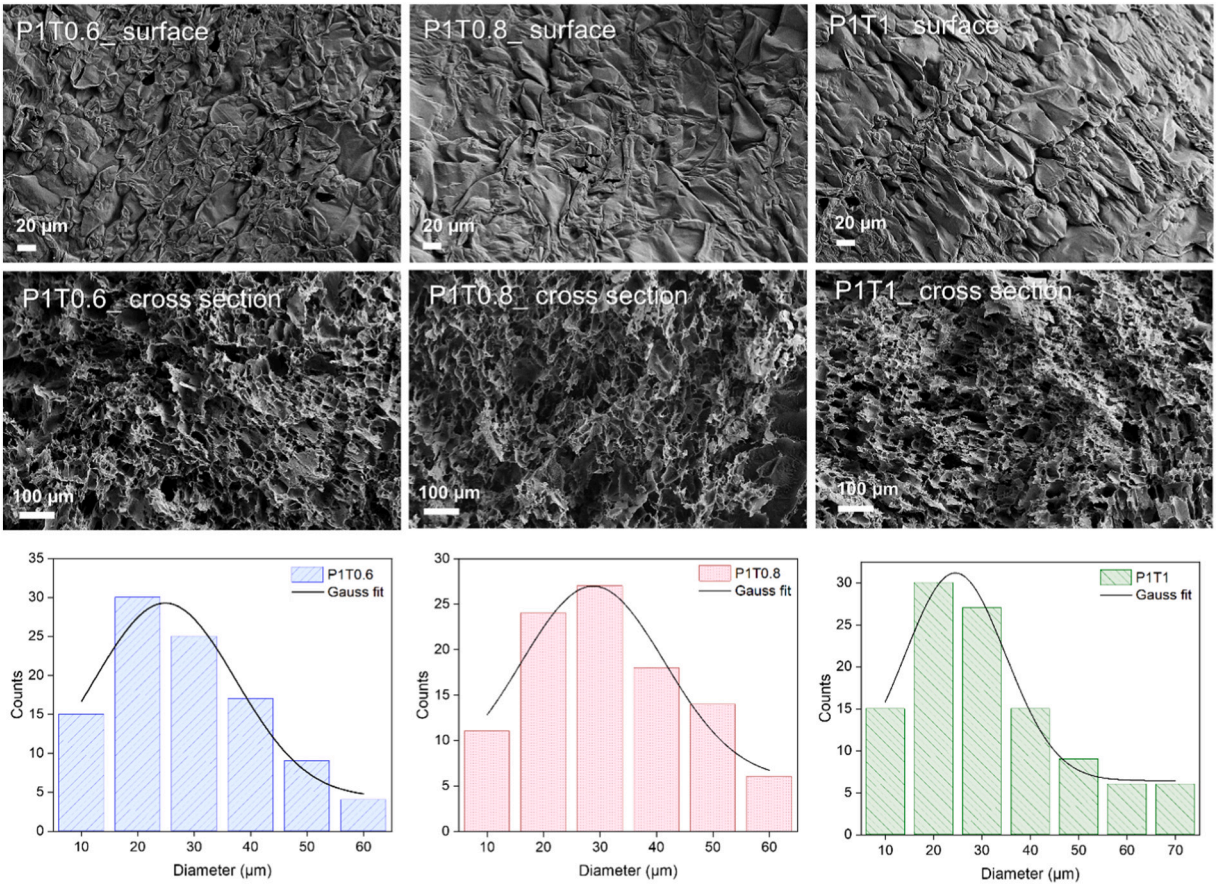

Fig. 3. SEM images (surface and cross-section area) and pore size distribution of each composition.

rad.s^{-1}. All samples illustrated a linear G′ and G″ up to 1% deformation, followed by a decrease in G′ and an increase in G″. The G″ began to decrease after the deformation reached a threshold and then intersected the G′ curve. Reducing moduli at higher shear strain values could be due to a breakdown or disruption of the elastic network formed by the cellulosic elements [80]. Accordingly, the shear strain of 0.1% was selected as a safe deformation rate for the linear viscoelastic region. Fig. 5b shows the frequency sweep results conducted between 0.01 and 100 rad.s^{-1} at a fixed shear strain of 0.1%. Both moduli were independent of the applied shear strain; furthermore, G′ was significantly higher than G″ over the tested frequency ranges indicating a solid- or gel-like behavior. Moreover, they enhanced with the increase in the CNF content; for instance, G′ elevated from 7.61 ± 0.28 kPa in P1T0.6 to 22.2 ± 1.01 kPa in P1T1, indicating the reinforcing effect of CNF. In addition, the elastic moduli (E) of the samples calculated using Eq. (3) were 22.83 ± 0.84, 34.85 ± 1.74, and 66.6 ± 3.03 kPa for P1T0.6, P1T0.8, and P1T1, respectively, in line with the values reported in the literature for PVA/CNF hydrogels [23,81]. These values also had good agreement with the elastic modulus of skin and soft tissues [82,83]. To ensure the integrity of the hydrogel during adhering to a tissue, it should mimic the mechanical properties of the target organ [84]; accordingly, all the developed, printed hydrogels passed the required mechanical properties for soft tissue engineering applications.

It is worth noticing that the viscoelastic trend of the lyophilized 3D-printed sample was similar to that previously observed for the inks, indicating that the 3D printing and freeze-drying did not significantly affect the inks viscoelastic behavior. Nevertheless, moduli values of the lyophilized 3D-printed samples were at least 10 orders of magnitude higher than the inks, suggesting the orientation of micro- and nano-size cellulose fibers while extruding out through the nozzle and also the advantage of freeze-drying on the improvement of mechanical properties of the PVA-based hydrogel. It has been reported that the freeze-drying of PVA aqueous solutions forms ice crystals inside the sample while the polymer chains are concentrated in the unfrozen liquid domains and interact with each other and consequently form a strong physical network structure [85,86].

The compressive test was conducted to further evaluate the mechanical properties of the developed hydrogels. The compressive stress-strain curves and the compressive modulus and stress at different strain levels are presented in Fig. 5c and d. Furthermore, the photographs of compressed and recovered samples are also depicted in Fig. 5e. The samples had good stability during the test and were not broken during the test. They presented a linear trend until 20% strain, then a pronounced enhancement after 30% strain, followed by a sharp increase in stress values after 60% strain. At the linear region, upon applying the stress, the relaxed hydrogel experienced a stressed state and began to an elastic deformation to store energy and resist the compressive stress. This deformation could be attributed to the loss of free water, which was not wholly entrapped in the hydrogel matrix. The significantly enhanced stress values after 30% strain could be due to reaching deformation to its limit value, making the subsequent deformation more difficult [87]. On the other side, considerable improvement was observed in compression mechanical properties upon increasing CNF content. For instance, at 30% strain, the compressive modulus and stress enhanced from 22.92 ± 1.12 kPa and 7.36 ± 0.32 kPa to 32.1 ± 1.27 kPa, and 10.81 ± 0.46 kPa, respectively. This improvement could be due to the increased hydrogen-bonded cross-linking density between free hydroxyl groups of PVA and CNF, allowing stress to transfer from the matrix to the reinforcement [88]. The compression modulus was in the range reported for soft tissues (0.3–220 kPa) [89]; furthermore, the obtained modulus and stress values were in line with other researcher results performed on PVA/cellulose hydrogels. For instance, the PVA/carboxymethyl chitosan/

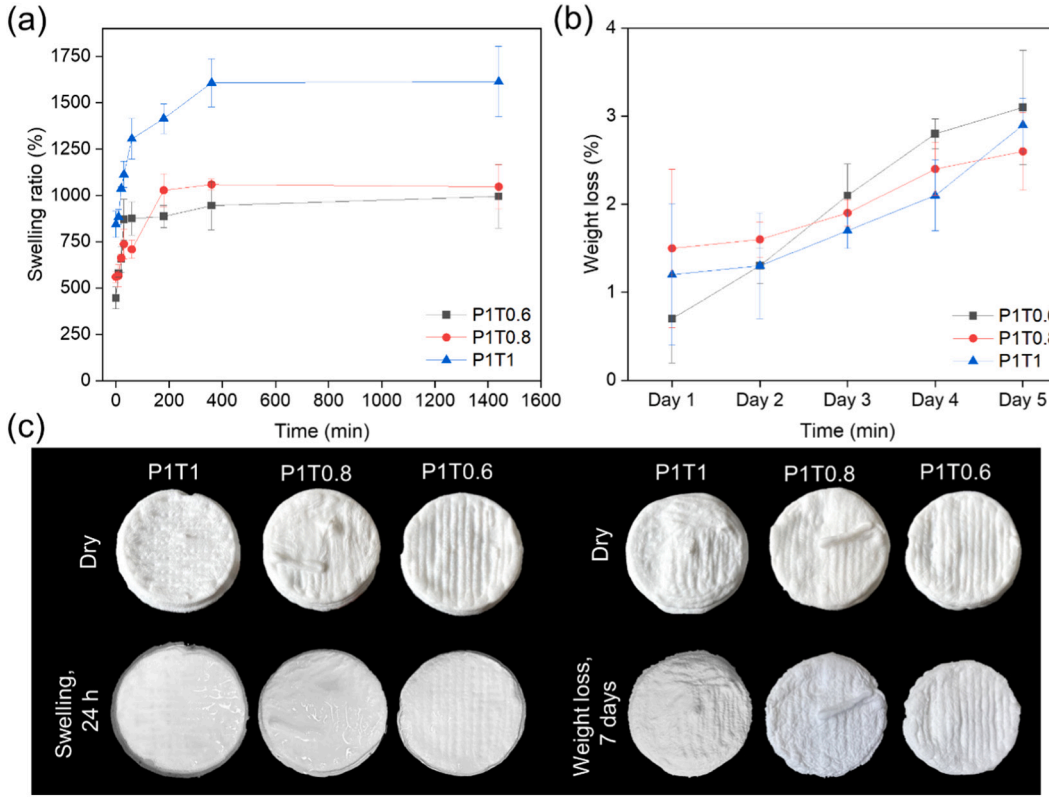

Fig. 4. (a) Swelling ratio and (b) weight loss of the lyophilized 3D-printed samples. (c) Digital photos of the freeze-dried, swelled (24 h), and degraded freeze-dried samples (7 days).

CNF hydrogel compression stress was reported as 37.7 kPa [90]. Furthermore, the compression stress at 60% strain was shown to be 100 kPa for CNC-reinforced PVA hydrogels [46]. Similarly, Tanpichai et al. [88] observed significant improvement in the mechanical properties of PAV/CNC hydrogels; namely, the compression strength increased from 17.5 kPa to 53 kPa in samples containing 1 wt% CNC.

3.6. Hydrogels composition

FTIR analysis was used to investigate the chemical structure of the developed hydrogels and confirm their compositions after freeze-drying. The FTIR spectra of pure PVA and CNF and composite hydrogels are provided in Fig. 6a. The characteristic peaks confirming PVA structure were as follows: -OH stretching band for the inter/intramolecular hydrogen bonds at 3300–3400 cm^{-1}, C—H alkyl stretching at 2850–3000 cm^{-1}, C═O and C—O stretching at 1710 cm^{-1} and shoulder at 1650 cm^{-1}, respectively, C-OH band at 1050–1150 cm^{-1}, and C—O band at 1090–1150 cm^{-1} [91,92]. On the other side, CNF illustrated the following characteristic peaks: a band near 1730 cm^{-1} corresponded to the C═O stretching of carboxyl groups, two peaks at 3361, 1635 cm^{-1} are attributed to OH stretching and OH bending, respectively [93]. These bans were detected in the spectra of hybrid hydrogels confirming hydrogel composition. Furthermore, no new peaks were detected at the fingerprint region of the composite hydrogels, which indicated the absence of a covalent bond between PVA and CNF and possibly an electrostatic interaction [93].

3.7. Ascorbic acid release study

It has been shown that ascorbic acid (vitamin C) can prevent and treat common colds and a number of illnesses, including respiratory infections. In addition, several studies have confirmed the positive impact of ascorbic acid on wound healing [29,94,95]. Accordingly, in the current study, ascorbic acid was loaded into the developed P1T1 hydrogel before and after 3D printing. The cumulative release profile of ascorbic acid is shown in Fig. 6b. A significant release (approximately 80%) was observed for the directly loaded drug during the first 8 h. It then produced a complete or near-complete release until the end of the test. Meanwhile, approximately 90% release was observed during 60 min for the indirectly loaded drug, in line with other reports [32]. This significant difference between release rates can be addressed considering the drug loading approaches and the drug release mechanism from hydrogels. The drug release from hydrogels can be divided into two parts: the release of surface drug and mesh-trapped drug. In the beginning, the drug-loaded hydrogel accommodates a minimum of water; therefore, the hydrogel exhibits minimum flexibility and small pore size. In this step, the release is more dominated by the solution of the drug molecules exposed to the surface. Accordingly, approximately 40% and 90% release was observed after 60 min for directly and indirectly loaded drug samples, respectively. This significant difference in release rate could be attributed to the loading method. Direct loading led to homogenous drug distribution throughout the sample, while in the indirect method, the drug was mostly absorbed in the sample surfaces; therefore, most of the loaded drugs were released at the beginning of the test. As time goes, water diffuses, and hydrogel undergoes relaxation to become more flexible, as previously observed in the swelling test results. This stage is accompanied by growing up of pore size and an increase in drug mobility, and consequently, the release of the entrapped drug is more predominant. This step could be considered between 1 and 4 h after the beginning of the test due to the swelling test results. Finally, the hydrogel is fully relaxed and hydrated, and the pore size reaches its maximum possible value, as is the rate of drug diffusion from the hydrogel [96,97]. The last two phases were more considerable for the directly loaded sample, in which the release increased from 40% to approximately 80% during 1 to 8 h after the beginning of the test, confirming a relatively slow release. A more prolonged release allows

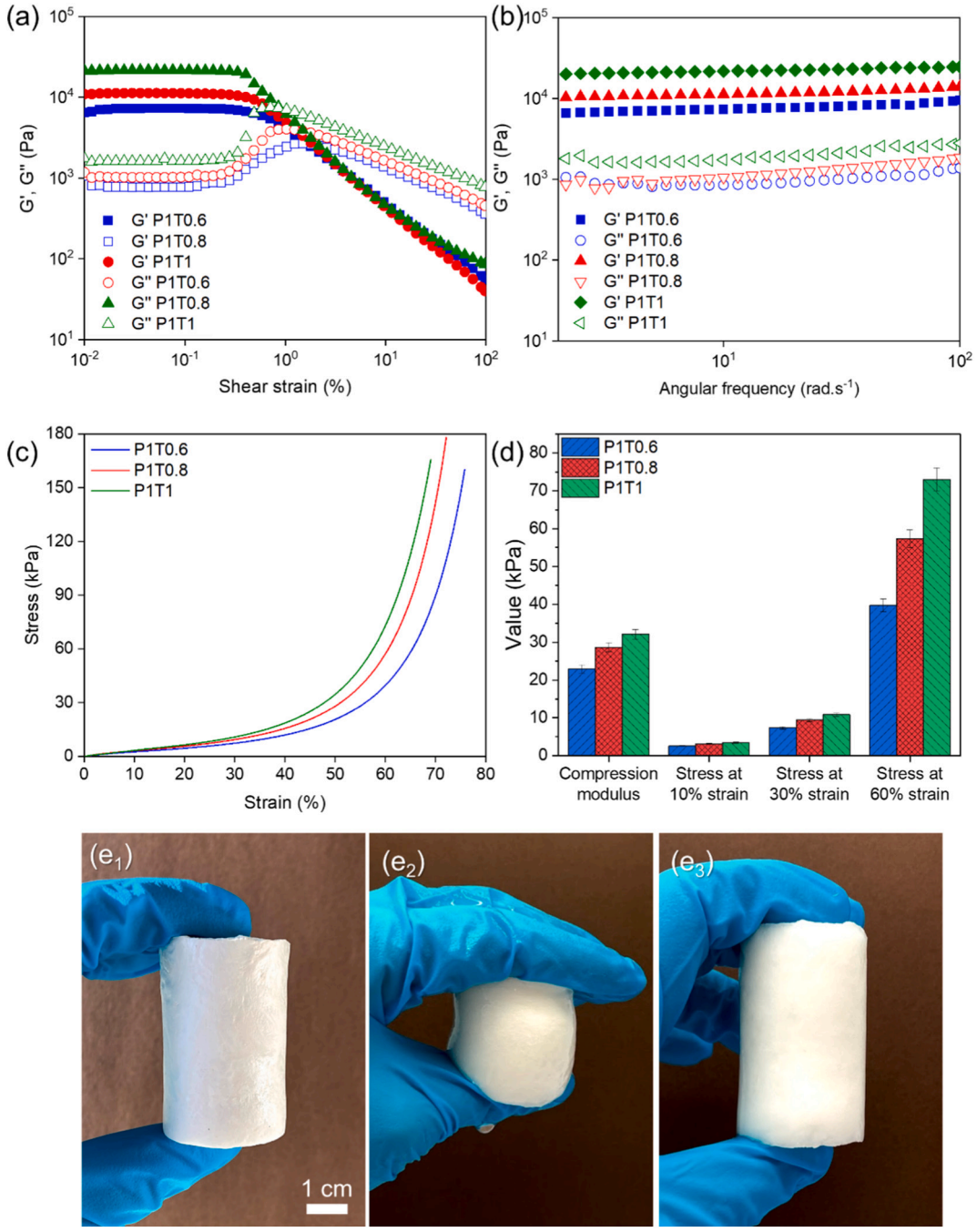

Fig. 5. (a) G′ and G″ versus strain rate from 0.01 to 100% at a fixed frequency of 10 rad.s^{-1} and (b) G′ and G″ versus frequency from 0.01 to 100 rad.s^{-1} at a fixed strain rate of 0.1%. (c) compression stress-strain and (d) compressive modulus and stress at different strain levels of rehydrated 3D-printed hydrogels. Photographs of (e_1) dry, (e_2) compressed wet sample, (e_3), and recovered wet structure after compression. The P1T1 hydrogel was poured into a Teflon mold (r and l = 17 and 50 mm, respectively) and freeze-dried. The lyophilized sample was swelled in PBS solution for 24 h prior to compression.

longer intervals of administrations, promoting patient compliance and comfort, enhances the therapeutic activity of ascorbic acid at the target, and reduces the risk of apoptosis at a high dose. Furthermore, the controlled and efficient delivery would be advantageous for a modern wound dressing [96,98].

4. Conclusion

We introduced polyvinyl alcohol/cellulose nanofibrils composite inks suitable for direct ink writing under ambient conditions. The PVA/CNF inks revealed a shear-thinning behavior under applied shear rate and excellent viscoelastic properties, which were more pronounced in samples with higher levels of CNF loading due to the formation of a physical network. All inks presented excellent flowability under printing conditions, with no evidence of needle clogging nor liquid spreading. The layers remained individualized (no signs of collapse) and maintained a uniform structure. Accordingly, 3D-lattice structures were printed with suitable resolution and high-shape fidelity. The freeze-dried 3D-printed samples revealed high porosity, with open and interconnected pores allowing a high swelling ratio (up to 1600%). Furthermore, they possessed excellent compression properties matching those of soft tissues. The structures provided efficient and controlled

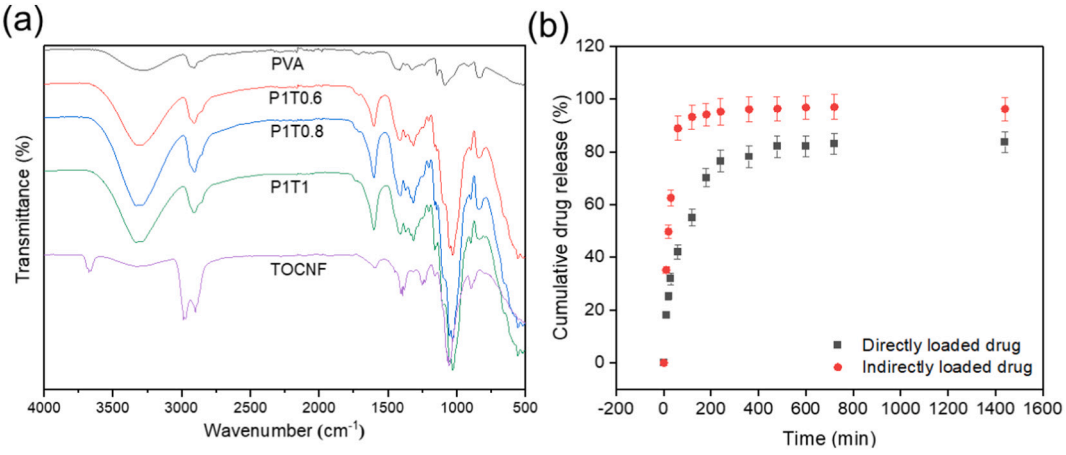

Fig. 6. (a) FTIR spectra of the freeze-dried samples and (b) ascorbic acid release profiles for the P1T1 sample.

release of ascorbic acid (up to 80% release within 8 h). Overall, the PVA/CNF 3D-geometries obtained by DIW showed a high porosity, water retention capacity, and mechanical performance compared to that of soft tissues.

CRediT authorship contribution statement

Hossein Baniasadi: Conceptualization, Methodology, Formal analysis, Investigation, Writing – original draft, Writing – review & editing, Visualization. **Zahraalsadat Madani:** Methodology, Formal analysis, Investigation. **Rubina Ajdary:** Conceptualization, Methodology, Formal analysis, Investigation, Writing – original draft, Writing – review & editing, Visualization. **Orlando J. Rojas:** Supervision, Funding acquisition, Writing – review & editing. **Jukka Seppälä:** Supervision, Funding acquisition, Writing – review & editing.

Declaration of competing interest

The authors declare that they have no known competing financial interests or personal relationships that could have influenced the work reported in this paper.

Acknowledgment

The authors would like to acknowledge the Academy of Finland funding; No. 327248 (ValueBiomat), 327865 (Bioeconomy), and 307485 (3DBiomat, 3D Manufacturing of Novel Biomaterials). This work made use of the facilities of Aalto University's Nanomicroscopy Center.

Appendix A. Supplementary data

Supplementary data to this article can be found online at https://doi.org/10.1016/j.msec.2021.112424.

References

[1] D. Podstawczyk, M. Niziol, P. Szymczyk, P. Wiśniewski, A. Guiseppi-Elie, 3D printed stimuli-responsive magnetic nanoparticle embedded alginate-methylcellulose hydrogel actuators, Addit. Manuf. 34 (2020), 101275.
[2] M. Hassan, K. Dave, R. Chandrawati, F. Dehghani, V.G. Gomes, 3D printing of biopolymer nanocomposites for tissue engineering: nanomaterials, processing and structure-function relation, Eur. Polym. J. 121 (2019), 109340, https://doi.org/10.1016/j.eurpolymj.2019.109340.
[3] M. Rajabi, M. McConnell, J. Cabral, M.A. Ali, Chitosan hydrogels in 3D printing for biomedical applications, Carbohydr. Polym. 260 (2021) 1–20.
[4] M. Zhang, A. Vora, W. Han, R.J. Wojtecki, H. Maune, A.B.A. Le, L.E. Thompson, G. M. McClelland, F. Ribet, A.C. Engler, Dual-responsive hydrogels for direct-write 3D printing, Macromolecules. 48 (2015) 6482–6488.
[5] P. Jiang, C. Yan, Y. Guo, X. Zhang, M. Cai, X. Jia, X. Wang, F. Zhou, Direct ink writing with high-strength and swelling-resistant biocompatible physically crosslinked hydrogels, Biomater. Sci. 7 (2019) 1805–1814.
[6] H. Baniasadi, R. Ajdary, J. Trifol, O.J. Rojas, J. Seppälä, Direct ink writing of Aloe vera/cellulose nanofibrils bio-hydrogels, Carbohydr. Polym. 266 (2021) 1–12.
[7] L. Li, Q. Lin, M. Tang, A.J.E. Duncan, C. Ke, Advanced polymer designs for direct-ink-write 3D printing, Chem. Eur. J. 25 (2019) 10768–10781.
[8] R. Ajdary, B.L. Tardy, B.D. Mattos, L. Bai, O.J. Rojas, Plant nanomaterials and inspiration from nature: water interactions and hierarchically structured hydrogels, Adv. Mater. (2020), 2001085, https://doi.org/10.1002/adma.202001085.
[9] S. Huan, B.D.B.D. Mattos, R. Ajdary, W. Xiang, L. Bai, O.J.O.J. Rojas, Two-phase emulgels for direct ink writing of skin-bearing architectures, Adv. Funct. Mater. (2019), 1902990, https://doi.org/10.1002/adfm.201902990.
[10] J. Li, C. Wu, P.K. Chu, M. Gelinsky, 3D printing of hydrogels: rational design strategies and emerging biomedical applications, Mater. Sci. Eng. R. Rep. 140 (2020), 100543, https://doi.org/10.1016/j.mser.2020.100543.
[11] S.E. Bakarich, R. Gorkin III, R. Gately, S. Naficy, M. in het Panhuis, G.M. Spinks, 3D printing of tough hydrogel composites with spatially varying materials properties, Addit. Manuf. 14 (2017) 24–30.
[12] M. Muchová, L. Münster, Z. Capáková, V. Mikulcová, I. Kuřitka, J. Vícha, Design of dialdehyde cellulose crosslinked poly(vinyl alcohol) hydrogels for transdermal drug delivery and wound dressings, Mater. Sci. Eng. C 116 (2020), 111242, https://doi.org/10.1016/j.msec.2020.111242.
[13] X.Y. He, A. Sun, T. Li, Y.J. Qian, H. Qian, Y.F. Ling, L.H. Zhang, Q.Y. Liu, T. Peng, Z. Qian, Mussel-inspired antimicrobial gelatin/chitosan tissue adhesive rapidly activated in situ by H2O2/ascorbic acid for infected wound closure, Carbohydr. Polym. 247 (2020), 116692.
[14] N. Shojarazavi, S. Mashayekhan, H. Pazooki, S. Mohsenifard, H. Baniasadi, Alginate/cartilage extracellular matrix-based injectable interpenetrating polymer network hydrogel for cartilage tissue engineering, J. Biomater. Appl. (2021) 1–15.
[15] H. Abou-Yousef, S. Dacrory, M. Hasanin, E. Saber, S. Kamel, Biocompatible hydrogel based on aldehyde-functionalized cellulose and chitosan for potential control drug release, Sustain. Chem. Pharm. 21 (2021), 100419.
[16] X. Chen, C. Chen, H. Zhang, Y. Huang, J. Yang, D. Sun, Facile approach to the fabrication of 3D cellulose nanofibrils (CNFs) reinforced poly(vinyl alcohol) hydrogel with ideal biocompatibility, Carbohydr. Polym. 173 (2017) 547–555, https://doi.org/10.1016/j.carbpol.2017.06.036.
[17] M. Baniasadi, H. Baniasadi, R. Azimi, N. Khosravi Dehaghi, Fabrication and characterization of a wound dressing composed of polyvinyl alcohol/nanochitosan/Artemisia ciniformis extract: An RSM study, Polym. Eng. Sci. 60 (2020), https://doi.org/10.1002/pen.25393.
[18] Y. Hussein, S.A. Loutfy, E.A. Kamoun, S.H. El-Moslamy, E.M. Radwan, S.E. I. Elbehairi, Enhanced anti-cancer activity by localized delivery of curcumin form PVA/CNCs hydrogel membranes: preparation and in vitro bioevaluation, Int. J. Biol. Macromol. 170 (2021) 107–122, https://doi.org/10.1016/j.ijbiomac.2020.12.133.
[19] A. Joorabloo, M.T. Khorasani, H. Adeli, Z. Mansoori-Moghadam, A. Moghaddam, Fabrication of heparinized nano ZnO/poly(vinylalcohol)/carboxymethyl cellulose bionanocomposite hydrogels using artificial neural network for wound dressing application, J. Ind. Eng. Chem. 70 (2019) 253–263, https://doi.org/10.1016/j.jiec.2018.10.022.
[20] A. Das, R. Uppaluri, C. Das, Compositional synergy of poly-vinyl alcohol, starch, glycerol and citric acid concentrations during wound dressing films fabrication, Int. J. Biol. Macromol. 146 (2020) 70–79, https://doi.org/10.1016/j.ijbiomac.2019.12.178.
[21] Y. Meng, J. Cao, Y. Chen, Y. Yu, L. Ye, 3D printing of a poly (vinyl alcohol)-based nano-composite hydrogel as an artificial cartilage replacement and the improvement mechanism of printing accuracy, J. Mater. Chem. B 8 (2020) 677–690.

[22] J. Yang, X. An, L. Liu, S. Tang, H. Cao, Q. Xu, H. Liu, Cellulose, hemicellulose, lignin, and their derivatives as multi-components of bio-based feedstocks for 3D printing, Carbohydr. Polym. 250 (2020) 1–16.
[23] X. Jing, H. Li, H.-Y. Mi, Y.-J. Liu, P.-Y. Feng, Y.-M. Tan, L.-S. Turng, Highly transparent, stretchable, and rapid self-healing polyvinyl alcohol/cellulose nanofibril hydrogel sensors for sensitive pressure sensing and human motion detection, Sensors Actuators B Chem. 295 (2019) 159–167.
[24] R. Ajdary, S. Huan, N. Zanjanizadeh Ezazi, W. Xiang, R. Grande, H.A. Santos, O. J. Rojas, Acetylated nanocellulose for single-component bioinks and cell proliferation on 3D-printed scaffolds, Biomacromolecules. 20 (2019) 2770–2778, https://doi.org/10.1021/acs.biomac.9b00527.
[25] X. Zhang, M. Morits, C. Jonkergouw, A. Ora, J.J. Valle-Delgado, M. Farooq, R. Ajdary, S. Huan, M. Linder, O. Rojas, M.H. Sipponen, M. Österberg, Three-dimensional printed cell culture model based on spherical colloidal lignin particles and cellulose nanofibril-alginate hydrogel, Biomacromolecules. 21 (2020) 1875–1885, https://doi.org/10.1021/acs.biomac.9b01745.
[26] R. Ajdary, N.Z. Ezazi, A. Correia, M. Kemell, S. Huan, H.J. Ruskoaho, J. Hirvonen, H.A. Santos, O.J. Rojas, Multifunctional 3D-printed patches for long-term drug release therapies after myocardial infarction, Adv. Funct. Mater. 30 (2020), https://doi.org/10.1002/adfm.202003440.
[27] S. Huan, R. Ajdary, L. Bai, V. Klar, O.J. Rojas, Low solids emulsion gels based on nanocellulose for 3D-printing, Biomacromolecules. 20 (2019) 635–644, https://doi.org/10.1021/acs.biomac.8b01224.
[28] I.M. Lourenço, M.T. Pelegrino, J.C. Pieretti, G.P. Andrade, G. Cerchiaro, A. B. Seabra, Synthesis, characterization and cytotoxicity of chitosan-coated Fe3O4 nanoparticles functionalized with ascorbic acid for biomedical applications, in: J. Phys. Conf. Ser, IOP Publishing, 2019, p. 12015.
[29] M.M. Hussain, A.M. Asiri, M.M. Rahman, Non-enzymatic simultaneous detection of acetylcholine and ascorbic acid using ZnO· CuO nanoleaves: real sample analysis, Microchem. J. 159 (2020), 105534.
[30] R. Ajdary, S. Huan, N. Zanjanizadeh Ezazi, W. Xiang, R. Grande, H.A. Santos, O. J. Rojas, Acetylated nanocellulose for single-component bioinks and cell proliferation on 3D-printed scaffolds, Biomacromolecules. 20 (2019), https://doi.org/10.1021/acs.biomac.9b00527.
[31] F. Damiri, Y. Bachra, C. Bounacir, A. Laaraibi, M. Berrada, Synthesis and characterization of lyophilized chitosan-based hydrogels cross-linked with benzaldehyde for controlled drug release, J. Chemother. 2020 (2020), https://doi.org/10.1155/2020/8747639.
[32] N. Ciftci, I. Sargin, G. Arslan, U. Arslan, A. Okudan, Ascorbic acid adsorption-release performance and antibacterial activity of chitosan-ter(GMA-MA-NTBA) polymer microcapsules, J. Polym. Environ. 28 (2020) 2277–2288, https://doi.org/10.1007/s10924-020-01773-0.
[33] N. Zandi, E.S. Sani, E. Mostafavi, D.M. Ibrahim, B. Saleh, M.A. Shokrgozar, E. Tamjid, P.S. Weiss, A. Simchi, N. Annabi, Nanoengineered shear-thinning and bioprintable hydrogel as a versatile platform for biomedical applications, Biomaterials. 267 (2021), 120476.
[34] T. Ma, L. Lv, C. Ouyang, X. Hu, X. Liao, Y. Song, X. Hu, Rheological behavior and particle alignment of cellulose nanocrystal and its composite hydrogels during 3D printing, Carbohydr. Polym. 253 (2021), 117217.
[35] O. Fourmann, M.K. Hausmann, A. Neels, M. Schubert, G. Nyström, T. Zimmermann, G. Siqueira, 3D printing of shape-morphing and antibacterial anisotropic nanocellulose hydrogels, Carbohydr. Polym. 259 (2021) 1–11.
[36] G. Siqueira, D. Kokkinis, R. Libanori, M.K. Hausmann, A.S. Gladman, A. Neels, P. Tingaut, T. Zimmermann, J.A. Lewis, A.R. Studart, Cellulose nanocrystal inks for 3D printing of textured cellular architectures, Adv. Funct. Mater. 27 (2017), https://doi.org/10.1002/adfm.201604619.
[37] H. Baniasadi, A. Ramazani S.A., S. Mashayekhan, Fabrication and characterization of conductive chitosan/gelatin-based scaffolds for nerve tissue engineering, Int. J. Biol. Macromol. 74 (2015) 360–366, https://doi.org/10.1016/j.ijbiomac.2014.12.014.
[38] C.T. Rueden, J. Schindelin, M.C. Hiner, B.E. DeZonia, A.E. Walter, E.T. Arena, K. W. Eliceiri, ImageJ2: ImageJ for the next generation of scientific image data, BMC Bioinformatics 18 (2017) 1–26.
[39] H. Pan, D. Fan, Z. Duan, C. Zhu, R. Fu, X. Li, Non-stick hemostasis hydrogels as dressings with bacterial barrier activity for cutaneous wound healing, Mater. Sci. Eng. C 105 (2019), 110118.
[40] S.A. Maniyar, J.G. Jargar, S.N. Das, S.A. Dhundasi, K.K. Das, Alteration of chemical behavior of L-ascorbic acid in combination with nickel sulfate at different pH solutions in vitro, Asian Pac. J. Trop. Biomed. 2 (2012) 220–222, https://doi.org/10.1016/S2221-1691(12)60045-8.
[41] K. Kiti, O. Suwantong, Bilayer wound dressing based on sodium alginate incorporated with curcumin-β-cyclodextrin inclusion complex/chitosan hydrogel, Int. J. Biol. Macromol. 164 (2020) 4113–4124, https://doi.org/10.1016/j.ijbiomac.2020.09.013.
[42] S.K. Romberg, M.A. Islam, C.J. Hershey, M. DeVinney, C.E. Duty, V. Kunc, B. G. Compton, Linking thermoset ink rheology to the stability of 3D-printed structures, Addit. Manuf. 37 (2020) 1–14.
[43] V. Kokol, Y.B. Pottathara, M. Mihelčič, L.S. Perše, Rheological properties of gelatine hydrogels affected by flow-and horizontally-induced cooling rates during 3D cryo-printing, Colloids Surf. A Physicochem. Eng. Asp. 616 (2021) 1–10.
[44] C.-C. Kuo, H. Qin, Y. Cheng, X. Jiang, X. Shi, An integrated manufacturing strategy to fabricate delivery system using gelatin/alginate hybrid hydrogels: 3D printing and freeze-drying, Food Hydrocoll. 111 (2021), 106262.
[45] Y. Cheng, H. Qin, N.C. Acevedo, X. Jiang, X. Shi, 3D printing of extended-release tablets of theophylline using hydroxypropyl methylcellulose (HPMC) hydrogels, Int. J. Pharm. 591 (2020), 119983.
[46] A.A. Moud, M. Kamkar, A. Sanati-Nezhad, S.H. Hejazi, U. Sundararaj, Viscoelastic properties of poly (vinyl alcohol) hydrogels with cellulose nanocrystals fabricated through sodium chloride addition: rheological evidence of double network formation, Colloids Surf. A Physicochem. Eng. Asp. 609 (2021), 125577, https://doi.org/10.1016/j.colsurfa.2020.125577.
[47] D. Liu, X. Dong, B. Han, H. Huang, M. Qi, Cellulose nanocrystal/collagen hydrogels reinforced by anisotropic structure: shear viscoelasticity and related strengthening mechanism, Compos. Commun. 21 (2020), 100374.
[48] H. Lee, J. You, H.-J. Jin, H.W. Kwak, Chemical and physical reinforcement behavior of dialdehyde nanocellulose in PVA composite film: a comparison of nanofiber and nanocrystal, Carbohydr. Polym. 232 (2020), 115771.
[49] A. Ounkaew, P. Kasemsiri, K. Jetsrisuparb, H. Uyama, Y.-I. Hsu, T. Boonmars, A. Artchayasawat, J.T.N. Knijnenburg, P. Chindaprasirt, Synthesis of nanocomposite hydrogel based carboxymethyl starch/polyvinyl alcohol/nanosilver for biomedical materials, Carbohydr. Polym. 248 (2020), 116767.
[50] H. Bian, L. Jiao, R. Wang, X. Wang, W. Zhu, H. Dai, Lignin nanoparticles as nano-spacers for tuning the viscoelasticity of cellulose nanofibril reinforced polyvinyl alcohol-borax hydrogel, Eur. Polym. J. 107 (2018) 267–274.
[51] J. Zhang, B.J. Allardyce, R. Rajkhowa, S. Kalita, R.J. Dilley, X. Wang, X. Liu, Silk particles, microfibres and nanofibres: A comparative study of their functions in 3D printing hydrogel scaffolds, Mater. Sci. Eng. C 103 (2019), 109784.
[52] B. Luo, H. Chen, Z. Zhu, B. Xie, C. Bian, Y. Wang, Printing single-walled carbon nanotube/Nafion composites by direct writing techniques, Mater. Des. 155 (2018) 125–133.
[53] M. Coffigniez, L. Gremillard, S. Balvay, J. Lachambre, J. Adrien, X. Boulnat, Direct-ink writing of strong and biocompatible titanium scaffolds with bimodal interconnected porosity, Addit. Manuf. 39 (2021) 1–15.
[54] P.T. Sudheesh Kumar, V.-K. Lakshmanan, T.V. Anilkumar, C. Ramya, P. Reshmi, A. G. Unnikrishnan, S.V. Nair, R. Jayakumar, Flexible and microporous chitosan hydrogel/nano ZnO composite bandages for wound dressing: in vitro and in vivo evaluation, ACS Appl. Mater. Interfaces 4 (2012) 2618–2629.
[55] S. Butylina, S. Geng, K. Oksman, Properties of as-prepared and freeze-dried hydrogels made from poly(vinyl alcohol) and cellulose nanocrystals using freeze-thaw technique, Eur. Polym. J. 81 (2016) 386–396, https://doi.org/10.1016/j.eurpolymj.2016.06.028.
[56] S. Plazzotta, S. Calligaris, L. Manzocco, Structure of oleogels from κ-carrageenan templates as affected by supercritical-CO2-drying, freeze-drying and lettuce-filler addition, Food Hydrocoll. 96 (2019) 1–10.
[57] H. Baniasadi, S.A. Ahmad Ramazani, S. Mashayekhan, M.R. Farani, F. Ghaderinezhad, M. Dabaghi, Design, Fabrication, and characterization of novel porous conductive scaffolds for nerve tissue engineering, Int. J. Polym. Mater. Polym. Biomater. 64 (2015). doi:https://doi.org/10.1080/00914037.2015.1038817.
[58] H. Lei, C. Zhu, D. Fan, Optimization of human-like collagen composite polysaccharide hydrogel dressing preparation using response surface for burn repair, Carbohydr. Polym. 239 (2020), 116249.
[59] S.A.P. Siboro, D.S.B. Anugrah, K. Ramesh, S.-H. Park, H.-R. Kim, K.T. Lim, Tunable porosity of covalently crosslinked alginate-based hydrogels and its significance in drug release behavior, Carbohydr. Polym. 260 (2021) 1–10.
[60] Z. Wang, F. Cheng, H. Cai, X. Li, J. Sun, Y. Wu, N. Wang, Y. Zhu, Robust versatile nanocellulose/polyvinyl alcohol/carbon dot hydrogels for biomechanical sensing, Carbohydr. Polym. 259 (2021) 1–9.
[61] R. Resmi, K.S. Anusree, R. Joseph, A. Bhatt, Scaffold for liver tissue engineering: exploring the potential of fibrin incorporated alginate dialdehyde-gelatin hydrogel, Int. J. Biol. Macromol. 166 (2020) 999–1008.
[62] A. Ahmed, M.B.K. Niazi, Z. Jahan, T. Ahmad, A. Hussain, E. Pervaiz, H.A. Janjua, Z. Hussain, In-vitro and in-vivo study of superabsorbent PVA/Starch/g-C3N4/Ag@TiO2 NPs hydrogel membranes for wound dressing, Eur. Polym. J. 130 (2020), 109650.
[63] J. Zhang, T. Liu, Z. Liu, Q. Wang, Facile fabrication of tough photocrosslinked polyvinyl alcohol hydrogels with cellulose nanofibrils reinforcement, Polymer (Guildf) 173 (2019) 103–109.
[64] K. Shi, X. Yang, J. Xu, D. Sha, B. Wang, X. Liu, Z. Liu, X. Ji, Preparation of polyvinyl alcohol formaldehyde-g-poly (2-(dimethylamino) ethyl methacrylate) macroporous hydrogels and their dual thermo/pH-responsive behavior and antibacterial performance, React. Funct. Polym. 164 (2021), 104916.
[65] S. Song, Z. Liu, M.A. Abubaker, L. Ding, J. Zhang, S. Yang, Z. Fan, Antibacterial polyvinyl alcohol/bacterial cellulose/nano-silver hydrogels that effectively promote wound healing, Mater. Sci. Eng. C 126 (2021), 112171.
[66] H. Li, C. Wu, S. Wang, W. Zhang, Mechanically strong poly (vinyl alcohol) hydrogel with macropores and high porosity, Mater. Lett. 266 (2020), 127504.
[67] R. Ghafari, M. Jonoobi, L.M. Amirabad, K. Oksman, A.R. Taheri, Fabrication and characterization of novel bilayer scaffold from nanocellulose based aerogel for skin tissue engineering applications, Int. J. Biol. Macromol. 136 (2019) 796–803.
[68] C.M. Murphy, F.J. O'Brien, Understanding the effect of mean pore size on cell activity in collagen-glycosaminoglycan scaffolds, Cell Adhes. Migr. 4 (2010) 377–381.
[69] K. Wang, J. Wang, L. Li, L. Xu, N. Feng, Y. Wang, X. Fei, J. Tian, Y. Li, Novel nonreleasing antibacterial hydrogel dressing by a one-pot method, ACS Biomater. Sci. Eng. 6 (2020) 1259–1268.
[70] P. Liu, K. Jin, W. Wong, Y. Wang, T. Liang, M. He, H. Li, C. Lu, X. Tang, Y. Zong, Ionic liquid functionalized non-releasing antibacterial hydrogel dressing coupled with electrical stimulation for the promotion of diabetic wound healing, Chem. Eng. J. 415 (2021) 1–13.

[71] L.Y. Maroufi, M. Ghorbani, Injectable chitosan-quince seed gum hydrogels encapsulated with curcumin loaded-halloysite nanotubes designed for tissue engineering application, Int. J. Biol. Macromol. 177 (2021) 485–494.
[72] M.B.K. Niazi, Z. Jahan, S.S. Berg, Ø.W. Gregersen, Mechanical, thermal and swelling properties of phosphorylated nanocellulose fibrils/PVA nanocomposite membranes, Carbohydr. Polym. 177 (2017) 258–268.
[73] Y. Guo, X. An, Z. Fan, Aramid nanofibers reinforced polyvinyl alcohol/tannic acid hydrogel with improved mechanical and antibacterial properties for potential application as wound dressing, J. Mech. Behav. Biomed. Mater. 118 (2021), 104452.
[74] H. Mert, B. Özkahraman, H. Damar, A novel wound dressing material: Pullulan grafted copolymer hydrogel via UV copolymerization and crosslinking, J. Drug Deliv. Sci. Technol. 60 (2020), 101962.
[75] B.A. Khan, A. Khan, M.K. Khan, V.A. Braga, Preparation and properties of high sheared poly(vinyl alcohol)/chitosan blended hydrogels films with Lawsonia inermis extract as wound dressing, J. Drug Deliv. Sci. Technol. (2020), 102227, https://doi.org/10.1016/j.jddst.2020.102227.
[76] A.M. Neres Santos, A.P. Duarte Moreira, C.W. Piler Carvalho, R. Luchese, E. Ribeiro, G.B. McGuinness, M. Fernandes Mendes, R. Nunes Oliveira, Physically cross-linked gels of PVA with natural polymers as matrices for manuka honey release in wound-care applications, Materials (Basel) 12 (2019) 559.
[77] O.J. Rojas, Cellulose Chemistry and Properties: Fibers, Nanocelluloses and Advanced Materials, Springer, 2016, https://doi.org/10.1007/978-3-319-26015-0.
[78] P. Date, A. Tanwar, P. Ladage, K.M. Kodam, D. Ottoor, Biodegradable and biocompatible agarose–poly (vinyl alcohol) hydrogel for the in vitro investigation of ibuprofen release, Chem. Pap. 74 (2020) 1965–1978.
[79] F. Hemmatgir, N. Koupaei, E. Poorazizi, Characterization of a novel semi-interpenetrating hydrogel network fabricated by polyethylene glycol diacrylate/polyvinyl alcohol/tragacanth gum as a wound dressing, Burns (2021), https://doi.org/10.1016/j.burns.2021.04.025.
[80] T. Moberg, K. Sahlin, K. Yao, S. Geng, G. Westman, Q. Zhou, K. Oksman, M. Rigdahl, Rheological properties of nanocellulose suspensions: effects of fibril/particle dimensions and surface characteristics, Cellulose. 24 (2017) 2499–2510, https://doi.org/10.1007/s10570-017-1283-0.
[81] G.K. Tummala, T. Joffre, R. Rojas, C. Persson, A. Mihranyan, Strain-induced stiffening of nanocellulose-reinforced poly (vinyl alcohol) hydrogels mimicking collagenous soft tissues, Soft Matter 13 (2017) 3936–3945.
[82] A. Kalra, A. Lowe, A.M. Al-Jumaily, Mechanical behaviour of skin: a review, J. Mater. Sci. Eng. 5 (2016), 1000254.
[83] J. Liu, H. Zheng, P.S.P. Poh, H.-G. Machens, A.F. Schilling, Hydrogels for engineering of perfusable vascular networks, Int. J. Mol. Sci. 16 (2015) 15997–16016.
[84] S. Mantha, S. Pillai, P. Khayambashi, A. Upadhyay, Y. Zhang, O. Tao, H.M. Pham, S.D. Tran, Smart hydrogels in tissue engineering and regenerative medicine, Materials (Basel) 12 (2019) 3323.
[85] M. Bercea, G. Biliuta, M. Avadanei, R.I. Baron, M. Butnaru, S. Coseri, Self-healing hydrogels of oxidized pullulan and poly(vinyl alcohol), Carbohydr. Polym. 206 (2019) 210–219, https://doi.org/10.1016/j.carbpol.2018.11.001.
[86] T. Abitbol, T. Johnstone, T.M. Quinn, D.G. Gray, Reinforcement with cellulose nanocrystals of poly (vinyl alcohol) hydrogels prepared by cyclic freezing and thawing, Soft Matter 7 (2011) 2373–2379.
[87] Y. Yue, J. Gu, J. Han, Q. Wu, J. Jiang, Effects of cellulose/salicylaldehyde thiosemicarbazone complexes on PVA based hydrogels: portable, reusable, and high-precision luminescence sensing of Cu2+, J. Hazard. Mater. 401 (2021), 123798.
[88] S. Tanpichai, K. Oksman, Cross-linked nanocomposite hydrogels based on cellulose nanocrystals and PVA: mechanical properties and creep recovery, Compos. A Appl. Sci. Manuf. 88 (2016) 226–233.
[89] Y. Kambe, Y. Mizoguchi, K. Kuwahara, T. Nakaoki, Y. Hirano, T. Yamaoka, Beta-sheet content significantly correlates with the biodegradation time of silk fibroin hydrogels showing a wide range of compressive modulus, Polym. Degrad. Stab. 179 (2020), 109240.
[90] M. Li, Q. Tu, X. Long, Q. Zhang, H. Jiang, C. Chen, S. Wang, D. Min, Flexible conductive hydrogel fabricated with polyvinyl alcohol, carboxymethyl chitosan, cellulose nanofibrils, and lignin-based carbon applied as strain and pressure sensor, Int. J. Biol. Macromol. 166 (2021) 1526–1534.
[91] D.N. Iqbal, S. Shafiq, S.M. Khan, S.M. Ibrahim, S.A. Abubshait, A. Nazir, M. Abbas, M. Iqbal, Novel chitosan/guar gum/PVA hydrogel: preparation, characterization and antimicrobial activity evaluation, Int. J. Biol. Macromol. 164 (2020) 499–509.
[92] S. Panpinit, S. Pongsomboon, T. Keawin, S. Saengsuwan, Development of multicomponent interpenetrating polymer network (IPN) hydrogel films based on 2-hydroxyethyl methacrylate (HEMA), acrylamide (AM), polyvinyl alcohol (PVA) and chitosan (CS) with enhanced mechanical strengths, water swelling and antibacteria, React. Funct. Polym. 156 (2020), 104739.
[93] T.H.M. Nguyen, C. Abueva, H. Van Ho, S.-Y. Lee, B.-T. Lee, In vitro and in vivo acute response towards injectable thermosensitive chitosan/TEMPO-oxidized cellulose nanofiber hydrogel, Carbohydr. Polym. 180 (2018) 246–255.
[94] I. Karakurt, A. Aydoğdu, S. Çıkrıkcı, J. Orozco, L. Lin, Stereolithography (SLA) 3D printing of ascorbic acid loaded hydrogels: a controlled release study, Int. J. Pharm. 584 (2020), 119428.
[95] C. Arab, R. El Kurdi, D. Patra, Chitosan coated zinc curcumin oxide nanoparticles for the determination of ascorbic acid, J. Mol. Liq. 328 (2021), 115504.
[96] J.C. Campos, D. Cunha, D.C. Ferreira, S. Reis, P.J. Costa, Oromucosal precursors of in loco hydrogels for wound-dressing and drug delivery in oral mucositis: retain, resist, and release, Mater. Sci. Eng. C 118 (2021), 111413.
[97] Y. Wang, J. Wang, Z. Yuan, H. Han, T. Li, L. Li, X. Guo, Chitosan cross-linked poly (acrylic acid) hydrogels: drug release control and mechanism, Colloids Surf. B: Biointerfaces 152 (2017) 252–259.
[98] S.M. Andrabi, S. Majumder, K.C. Gupta, A. Kumar, Dextran based amphiphilic nano-hybrid hydrogel system incorporated with curcumin and cerium oxide nanoparticles for wound healing, Colloids Surf. B: Biointerfaces 195 (2020) 111263.